INL/RPT-22-68401-Revision-0

Quarterly Management Document FY22, 3rd Quarter, Multi-pass Hybrid Laser Arc Welding of Alloy 740H

September 2022

Thomas M Lillo, Tate Patterson, Todd Palmer

Changing the World's Energy Future

Idaho National Laboratory

INL is a U.S. Department of Energy National Laboratory operated by Battelle Energy Alliance, LLC

INL/RPT-22-68401-Revision-0

Quarterly Management Document FY22, 3rd Quarter, Multi-pass Hybrid Laser Arc Welding of Alloy 740H

Thomas M Lillo, Tate Patterson, Todd Palmer

September 2022

Idaho National Laboratory
Idaho Falls, Idaho 83415

http://www.inl.gov

Prepared for the
U.S. Department of Energy
Under DOE Idaho Operations Office
Contract DE-AC07-05ID14517

Quarterly Management Document – FY22, 3rd Quarter, Multi-pass Hybrid Laser Arc Welding of Alloy 740H

Document # INL/RPT-22- 68401

WBS Element	**Project Title**	**Contract Number**	**Contract Start**	**Contract End**
C.B.75.AA.01.01.01	Multi-pass Hybrid Laser Arc Welding of Alloy 740H	B100-19010	**10/01/19**	**09/30/2022**

Performer Name and Address	**Principal Investigator(s)**
Thomas Lillo Idaho National Laboratory P.O. Box 1625 Idaho Falls, ID 83415	Thomas Lillo

BUDGET AND COST REPORT

Prior Year Funds ($K)				**68.4**								
Total Current Year Commitment ($K)				**502.4**								
Projected Current Year Costs ($K)				**502.4**								
	O	**N**	**D**	**J**	**F**	**M**	**A**	**M**	**J**	**J**	**A**	**S**
Monthly Planned Costs	**12**	**12**	**12**	**26**	**56.2**	**71.2**	**47.0**	**64.1**	**54.1**	**53.0**	**47.0**	**47.0**
Actual Monthly Costs	**10.1**	**18.2**	**13.0**	**16.6**	**45.5**	**54.0**	**55.4**	**28.9**	**30.4**			
Monthly Variance	**1.9**	**-6.2**	**-1.0**	**9.4**	**10.7**	**17.2**	**-8.4**	**35.2**	**23.7**			
Total costs – planned	**12**	**24**	**36**	**62**	**118.2**	**189.4**	**236.4**	**300.5**	**354.6**	**407.6**	**454.6**	**501.6**
Total costs - actual	**10.1**	**28.3**	**41.3**	**57.9**	**103.4**	**157.4**	**212.8**	**241.7**	**272.1**			

MILESTONE REPORT

Milestone Designation	Milestone Description	Due Date	Revised Due Date	Completion Date
Task 1	Purchase and installation of Laser Wobble Head at INL and PSU	12/31/2019	3/15/2020	6/31/2020
Task 2	Single pass bead-on-plate welds with microstructure characterization – Effect of Laser Wobble Modes during HLAW	12/2020		12/30/2020
Task 3	Deep Penetration Land Welding Development and Optimization of Multi-pass HLA welds	7/2021	12/2021	01/10/2022
Task 4	Modeling of Deep Penetration Laser Welding	9/2021	9/2022	
Go/No Go Decision Pt #1	Performance of Deep Penetration Land Welds and HLAW filler weld material	7/2021	09/2022	
Go/No Go Decision Pt #2	Cycle time evaluation for thick land/HLAW thick (~1.25”) welds and their performance	12/2021	10/2022	
Task 5	Complete 3” thick weld (thick land laser weld + HLAW groove filling)	6/2022	12/2022	
Task 6	Characterization – Microstructure & Mechanical properties of 3” thick weld	9/30/2022	12/2022	

TECHNICAL HIGHLIGHTS

Task 1, Purchase and installation of Laser Wobble Head at INL and PSU

Completed.

Task 2, Single pass bead-on-plate welds with microstructure characterization – Effect of Laser Wobble Modes during HLAW

Completed.

Task 3, Deep Penetration Land Welding Development and Optimization of Multi-pass HLA welds

Completed

Task 4, Modeling of Deep Penetration Laser Welding

Results on Laser keyhole mode welding of IN 740H (without wobble)

The recent publication of high-power keyhole mode laser welds in IN 740H [1] has shown that solidification cracks are common inside the finger region of the keyhole welds. An easy-to-calculate, vulnerable-to-relaxation time ratio was able to uncover the role of process parameters with cracking along with predicting the depth of cracking. However, the above solidification crack model could not comment on the orientation of cracks that appear in the welds. This needs an explicit stress state model, and this is explored in this section of the report.

The spatial variation in the stress state across the liquid/solid two-phase region was captured using a Standard/Explicit finite element analysis model in Abaqus®[1]. The calculation domain was 80 mm, 20 mm, and 12.7 mm in X, Y, and Z directions, as shown in **Fig.1**, and the mesh sizes are between 200 µm and 500 µm, with finer meshes in the molten pool and coarser meshes in the pure solid region. The temperature field calculated from the heat transfer and fluid flow model was imported to the stress calculation model using a point cloud file through the analytical mapped fields function in Abaqus, and the temperature values on the nodes for the finite element model were automatically defined by inverse distance weighted method using the surrounding source points [2], as shown in **Fig 1**. Much finer meshes were used in the heat transfer and fluid flow model (1600788 elements) than the stress calculation model (77520 elements), and, therefore, a minimal error in the mapped temperature field is expected. The XZ plane where Y = 0 mm was a symmetric plane, and the XY plane where Z = 0 mm was taken as a free plane, which means it can deform freely. No displacement or rotation is allowed on the remaining four planes since the calculation domain is part of the big plate and these planes were surrounded by base metal during welding.

[1] Abaqus Inc, Palo Alto, CA, USA

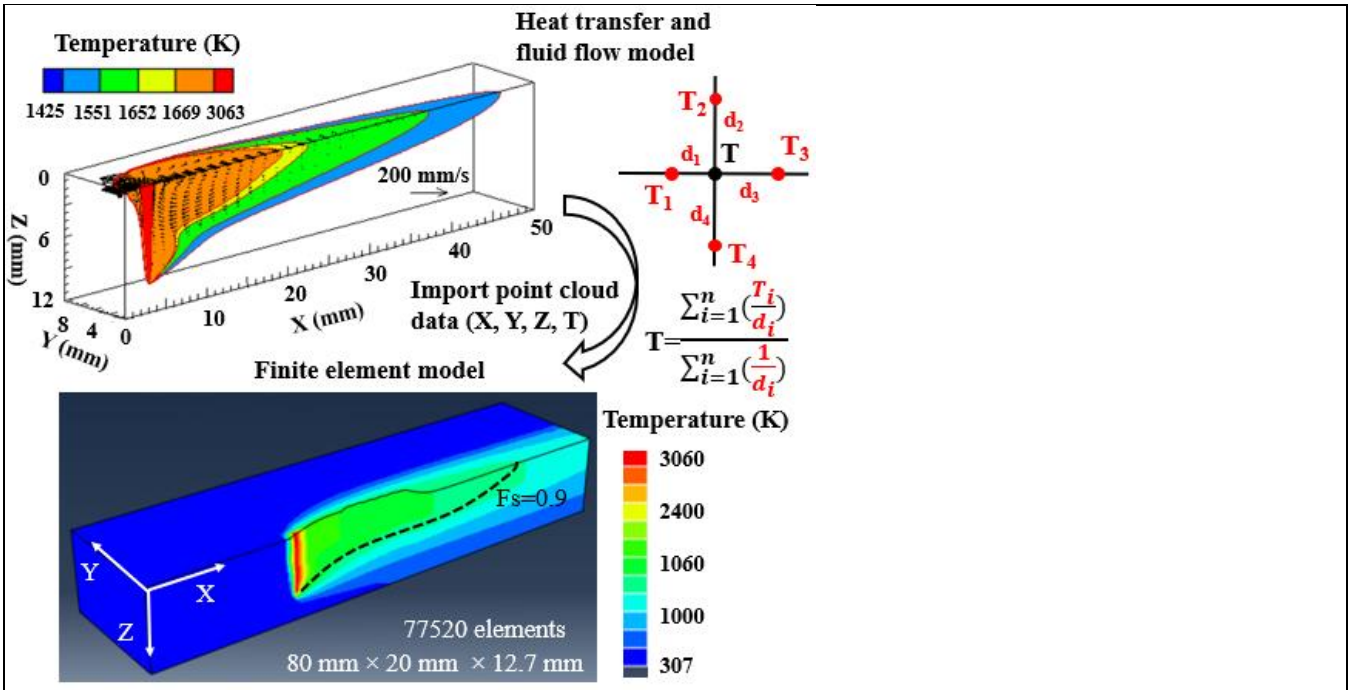

Fig. 1. Demonstration of importing the temperature field from heat transfer and fluid flow model into finite element model using a point cloud file. The temperature T on a node in finite element model was automatically determined by inverse distance weighted method using the surrounding source points. The domain size was 80 mm × 20 mm × 12.7 mm with 77520 elements in total.

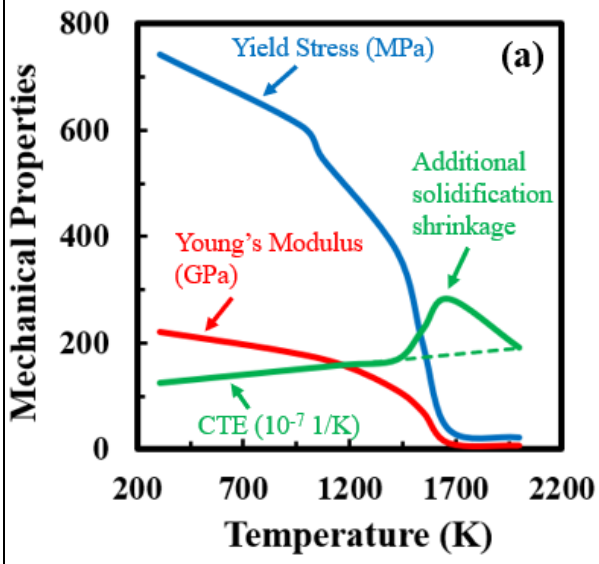

Fig. 2. (a) Temperature dependent material properties of Inconel 740H

The temperature-dependent mechanical properties of the alloys needed for the stress state calculation were taken from experimental measurements provided by the alloy manufacturer [3] and are shown in **Fig 2**. For the temperatures above liquidus temperature, Young's modulus and yield strength were assumed as 3% of the values at room temperature to account for the soft nature of the liquid (this value prevents

stress from developing in the liquid during the simulation but is sufficient to allow the simulation solution to converge). Due to lack of data, perfect plasticity without work hardening is assumed. This assumption is reasonable since hardening is limited at high temperatures during solidification due to the rapid dislocation motion [4]. Additionally, the volumetric shrinkage during solidification can come from both thermal and solidification shrinkage, which is around 1.64% for nickel alloys with 24.5 wt% of Cr [5], similar to the compositions of Inconel 740H. Assuming the shrinkage is equal in all the directions, the calculated linear shrinkage is approximately 0.55%. Divided by solidification temperature range (244 K), the average linear coefficient of expansion between liquidus and solidus temperatures can be taken as 2.25×10^{-5} K^{-1}, and this coefficient was assumed to vary linearly within the solidification temperature range.

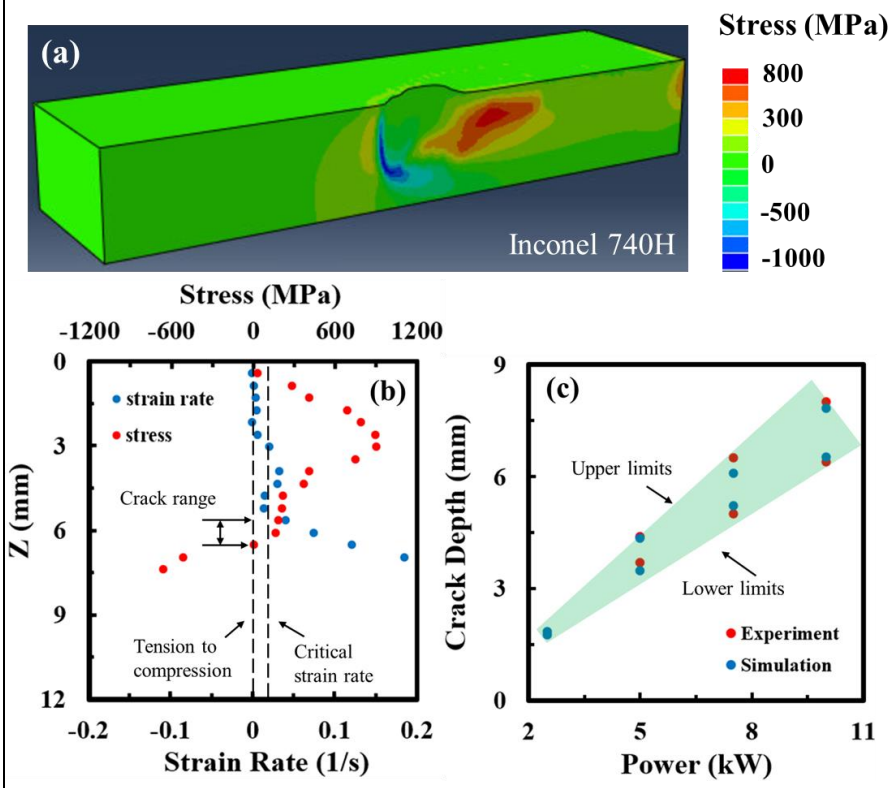

Fig. 3. (a) Vertical stress distribution of Inconel 740H. (b) The variation of effective stress and strain rate values along weld depth at fs=0.9 were shown for laser power of 7.5 kW and welding speed of 12.7 mm/s. (c) Comparison of experimentally measured and numerically calculated crack depths defined by the critical strain rate (lower limits) and the tension to compression transition point (upper limits) for Inconel 740H under different laser powers. The crack range was roughly represented by the green band.

It has been confirmed by welding experiments that a minimal strain rate needs to be attained to initiate solidification cracking, which is between 0.011 to 0.019 s^{-1} for other nickel alloys [6-7]. Since such data does not exist for Alloy 740H, the critical strain rate was thus taken, conservatively, as 0.019 s^{-1}, and, furthermore, solidification cracking is assumed only to occur at locations where the local strain rate is considerably higher (~>2x) than this value. As indicated in **Fig 3(b)**, the strain rate becomes significantly

greater than the critical strain at depths greater than ~5.2 mm for Inconel 740H, using laser power of 7.5 kW. Additionally, tensile stress is required for the crack to propagate, and no crack is likely to appear where the stress is compressive. The transition points from tension to compression are at depths of around 6.1 mm for laser power of 7.5 kW.

Solidification cracking is likely to appear at depths where both the critical strain rate is exceeded, and tensile stress is present. Thus, the range of depth associated with the formation of solidification cracks is approximately 0.9 mm for Inconel 740H at a laser power of 7.5 kW (i.e., the "crack range" indicated on Fig. 3b). The calculated ranges of crack depths and the experimentally determined crack depths for Inconel 740H under different laser powers are compared and shown in **Fig 3(c)**. The lower limit is determined by the critical strain rate and the upper limit is the tension to the compression transition point, and reasonable agreements were achieved between simulation and experiment.

Wobble model development

Laser wobble modeling (without keyhole) with movement of laser head in a circular trajectory is developed. A transient heat transfer and fluid flow model of the laser wobble welding solves the equation of mass, momentum, and energy in 3D to calculate the temperature and velocity fields.

Assuming a laser beam of radius 'r' moving along a circular trajectory with amplitude 'A', welding speed V_f, frequency 'f', the location of the laser source at any instant is given by

$$x = \frac{A}{2} cos \frac{2V_t}{A} t + V_f t \quad (1)$$

$$y = \frac{A}{2} sin \frac{2V_t}{A} t \quad (2)$$

where V_t is the tangential speed and is given by $V_t = f * \pi * A$ and 't' is the time.

The combined rotation of the laser beam with frequency 'f' along with forward movement with welding speed (V_f) generates a cycloid as shown in Fig 1. Here the laser rotates in anticlockwise direction starting at position 's' and follows points 't', 'u', 'v' before ending at position 'w' to start the second circle.

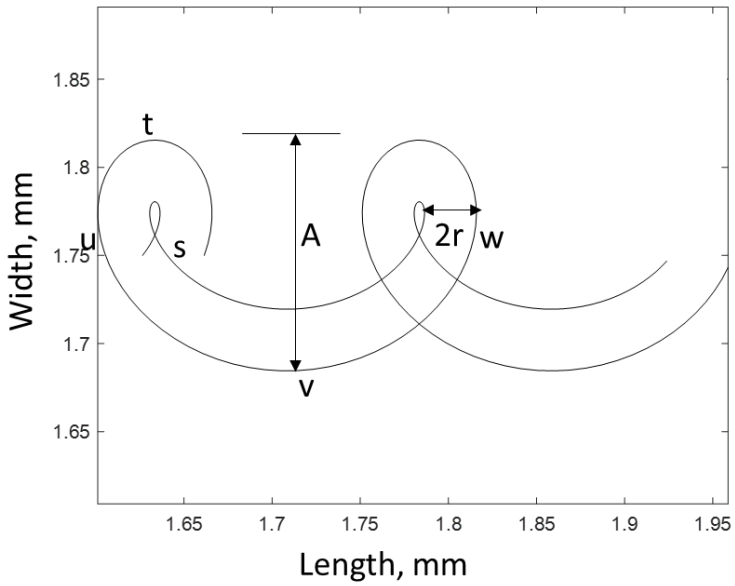

Fig. 4. Schematic of movement of laser source in a circular wobble trajectory with amplitude "A' for a path encircling two cycles. The laser starts at a position 's' and rotates counterclockwise tracing the path of 'stuvw'. Position 'w' marks the start position of the second cycle.

The laser wobble results in unique spatio-temporal evolution of temperature and pool. Earlier we had explored the spatial evolution of pool geometry at different locations of the circular trajectory. In this report we will explore the temporal evolution of the temperature fields and pool volume.

Using process parameters as listed below in table 1, simulations for some representative cases, named Case a, Case b, and Case c, were made and the corresponding plots of peak temperature distribution for wobble consisting of six circles are shown in Fig 5. We find that the peak temperature follows a sinusoidal nature varying between a minimum and maximum value for each of the cases. This is according to the relation described by equation (1) and (2). Referring to Fig 4, at a location between 't' and 'u' which is approaching closer to 'u' the first peak temperature, i.e maximum temperature in Fig. 5, is observed. Then when traversing the path "uv" at a location near 'v' the first minimum temperature in Fig. 5 is observed. This pattern of peak temperature repeats similarly for each laser wobble cycle.

Table 1: Process parameters used for circular laser wobble simulation

Parameters	**Case a**	**Case b**	**Case c**
Laser power (W)	250	250	250W
Welding speed (cm/s)	30	30	30
Laser radius (cm)	0.0035	0.0035	0.0035
Amplitude (cm)	0.0103	0.0103	0.0206
Frequency (Hz)	1000	2000	2000
Laser distribution	Gaussian	Gaussian	Gaussian

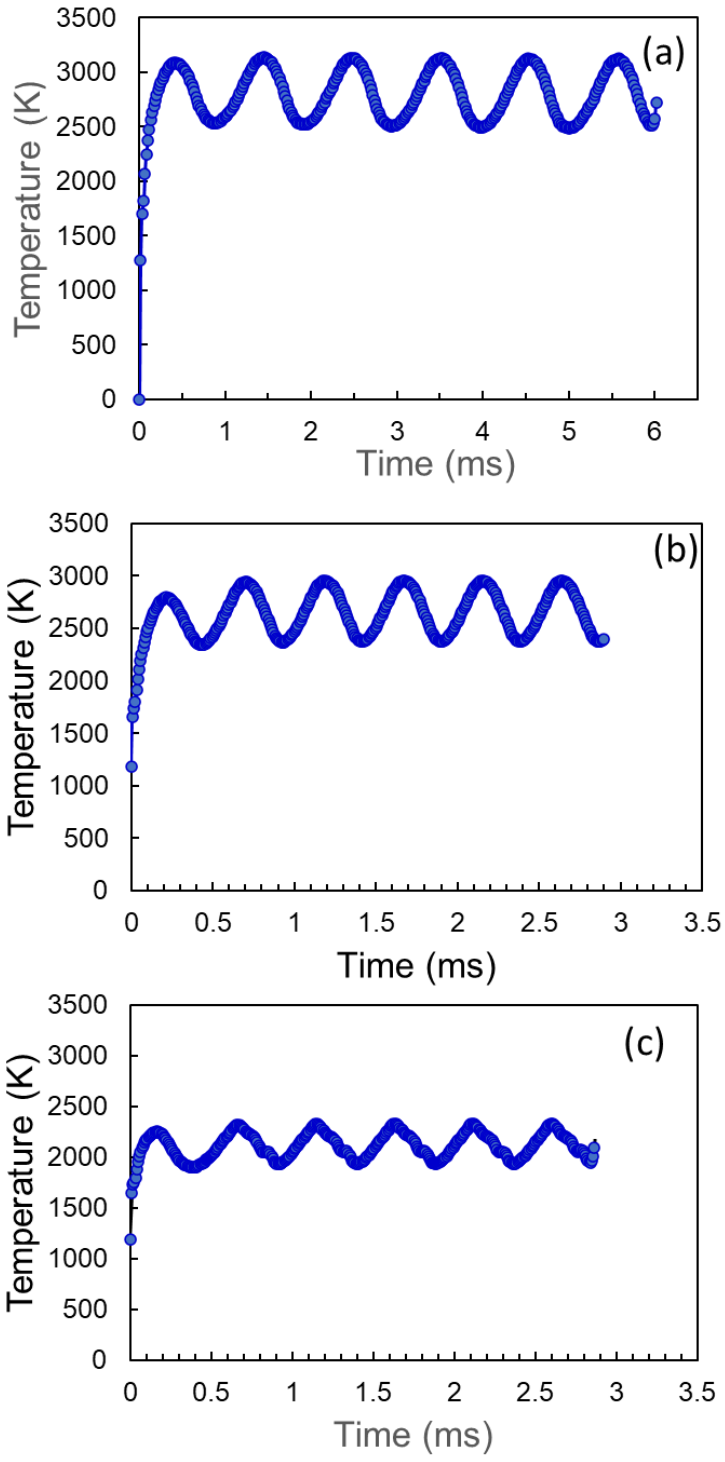

Fig. 5. Plot of temperature for (a) Case a (b) Case b (c) Case c.

While all three cases shown in Fig 5 have similar pattern the following differences are easy to observe

a. Increasing the frequency reduces the peak temperature. It is seen that 'Case b' with 2000 Hz frequency has lower peak temperature distribution of 2793 K compared to temperature of 3050 K for 'Case a' made at 1000 Hz frequency. Increasing frequency means the laser spends less time to scan the same number of circles and less laser-material interaction time results in a lower peak temperature,
b. Increasing the wobble amplitude decreases the peak temperature. Case c with 0.0206 cm wobble amplitude has peak temperature of 2300K compared to 2793 K for Case b with wobble amplitude of 0.0103 cm. Laser is being distributed over a larger area resulting in a lower peak temperature.

Additionally, pool volume was extracted from the transient heat transfer and fluid flow model and similar trends in pool volume was observed for the above three cases. However, when pool volume and peak temperature are superimposed, it is seen that the peak pool volume lags behind the peak temperature. Referring to Fig 4 once more, the peak pool volume occurs on the path of "uv" closer to u after the laser has crossed point "u". Pool volume lags behind peak temperature due to finite thermal diffusivity and heat capacity considerations.

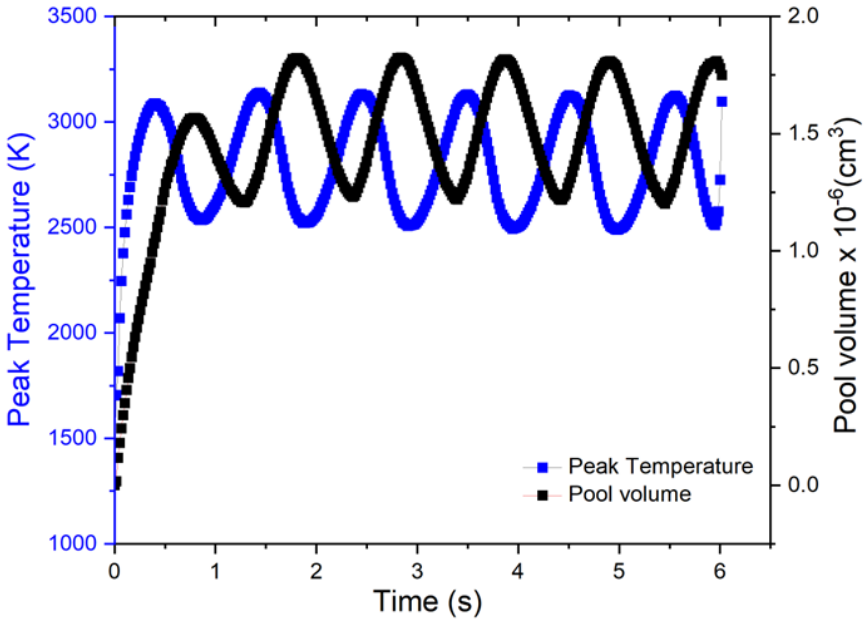

Fig. 6. Plot of pool peak temperature and pool volume for case b shows that the peak temperature lags behind the pool volume.

The unique pool geometry, spatio-temporal evolution of temperature (with velocity fields) and pool volume will affect the solidification parameters and, thus, can provide an interesting pathway for microstructure and property control.

References

1. Mondal B, Gao M, Palmer TA, DebRoy T. Solidification cracking of a nickel alloy during high-power keyhole mode laser welding. J Mater Process Technol. 2022;305(3):117576.
2. Smith M. Abaqus/CAE User's Manual, Version 6.12. Dassault Systemes Simulia Corp., Providence, RI, USA. 2012
3. Specialmetals. https://www.specialmetals.com/documents/technical-bulletins/inconel/inconel-alloy-740h.pdf. 2014
4. Semiatin SL, Mahaffey DW, Tung DJ, Zhang W, Senkov ON. A Comparison of the Plastic-Flow Response of a Powder-Metallurgy Nickel-Base Superalloy Under Nominally-Isothermal and Transient-Heating Hot-Working Conditions. Metall Mater Trans A Phys Metall Mater Sci. 2017;48(4):1864–79.
5. Xiao F, Yang R, Fang L, Zhang C. Solidification shrinkage of Ni-Cr alloys. Mater Sci Eng B Solid-State Mater Adv Technol. 2006;132(1–2):193–6.
6. Xia C, Kou S. Evaluating susceptibility of Ni-base alloys to solidification cracking by transverse-motion weldability test. Sci Technol Weld Join. 2020;25(8):690–7.
7. Coniglio N, Cross CE. Initiation and growth mechanisms for weld solidification cracking. Int Mater Rev. 2013;58(7):375–97

Update on Go/No Go Decision Pt #1: Performance of Deep Penetration Land Welds and HLAW filler weld material

In the previous two quarterly reports, it was declared that suitable HLAW parameters had been found that resulted in defect-free welds as shown in a transverse optical metallography sample of the weld Fig. 7. Short-term, as well as long-term, creep behavior of this weld was at least equivalent to that of conventional GTA welds and further supported this contention. However, during the preparation of a manuscript for a peer-reviewed publication, additional transverse sections of the weld were prepared for metallography, Fig. 8, to further support the contention that a defect-free weld had, indeed, been made. Unfortunately, these subsequent metallographic sections did reveal the presence of both liquation as well as solidification cracks. Even though they were small and few in number, their mere presence is considered a failed weld under the criteria outlined in the ASME Boiler and Pressure Vessel code.

The discovery of critical weld defects will force additional welding trials with variation of welding parameters as well as modifications to the HLAW configuration. However, significant progress has been made with each new welding campaign made during the project. Figure 9 shows this progress as decreasing amounts of solidification cracking with each successive welding campaign. Furthermore, the total solidification crack length appears to be a strong function of heat input (arc plus laser energy), Fig. 10. Although, we've achieved significant reduction in the total length of the liquation cracks (which, overall, are much less prevalent in the welds), the parameters affecting the liquation crack content is not clear at this time, also Fig. 10.

Laser Trailing

To mitigate cracking, attempts were made to perform HLAW with the laser trailing the arc, i.e., the laser is located behind the arc. The rationale was that in the laser trailing configuration, the wobbling laser would disrupt the solidifying weld and supply liquid melt to "heal" cracks that developed during solidification while keeping the heat input low enough to prevent liquation cracks. The system setup remained the same as with the laser leading the arc, but the travel direction was reversed, effectively resulting in the laser following behind the arc. The star wobble pattern was used with the same parameters as in Weld 11116, and the travel speed was 20 ipm. The contact-tip-to-work (CTWD) was reduced for improved arc stability, and the shielding gas flow rate was increased to 45 CFH to reduce oxidation and scale formation. The laser trailing configuration was expected to change the weld pool fluid flows and alter the microstructure evolution to mitigate solidification cracking.

In welds made using laser powers of 2 kW and 3 kW, weld defects were present as shown in Fig. 11 and 12, respectively. However, heat affected zone (HAZ) or weld metal liquation cracks were not identified in the cross-sections evaluated. For the 2 kW laser power, there was a single lack of fusion defect and a single solidification crack, Fig. 11. The 3 kW laser weld showed no lack of fusion but contained a single solidification crack, Fig. 12. Higher heat input generally improves resistance to lack of fusion, so it was believed that the 3 kW laser weld was less susceptible. Because solidification cracks were present in the laser trailing sections, it was difficult to correlate an improvement. However, the solidification crack lengths of 400 and 800 μm indicate similar characteristics as weld Campaign 3, Fig. 9. Because the laser beam is entirely orientated within the weld pool developed by the arc, this laser configuration has minimal influence in drastically stirring the weld pool – primarily only influencing arc stabilization.

Potential Solutions

Solutions that may eliminate the weldability issues experienced with the previous weld parameters include decoupling the laser from the arc or preheating the base material to reduce residual stresses. These approaches are further explained in the following subsections.

Fig. 7. First serial section of weld, Z11116, exhibiting a planar section without defects that would cause the weld to fail under the criteria of ASME Boiler and Pressure Vessel code, Section IX. (A few small pores are present but are not considered a failing defect according to the ASME code criteria.)

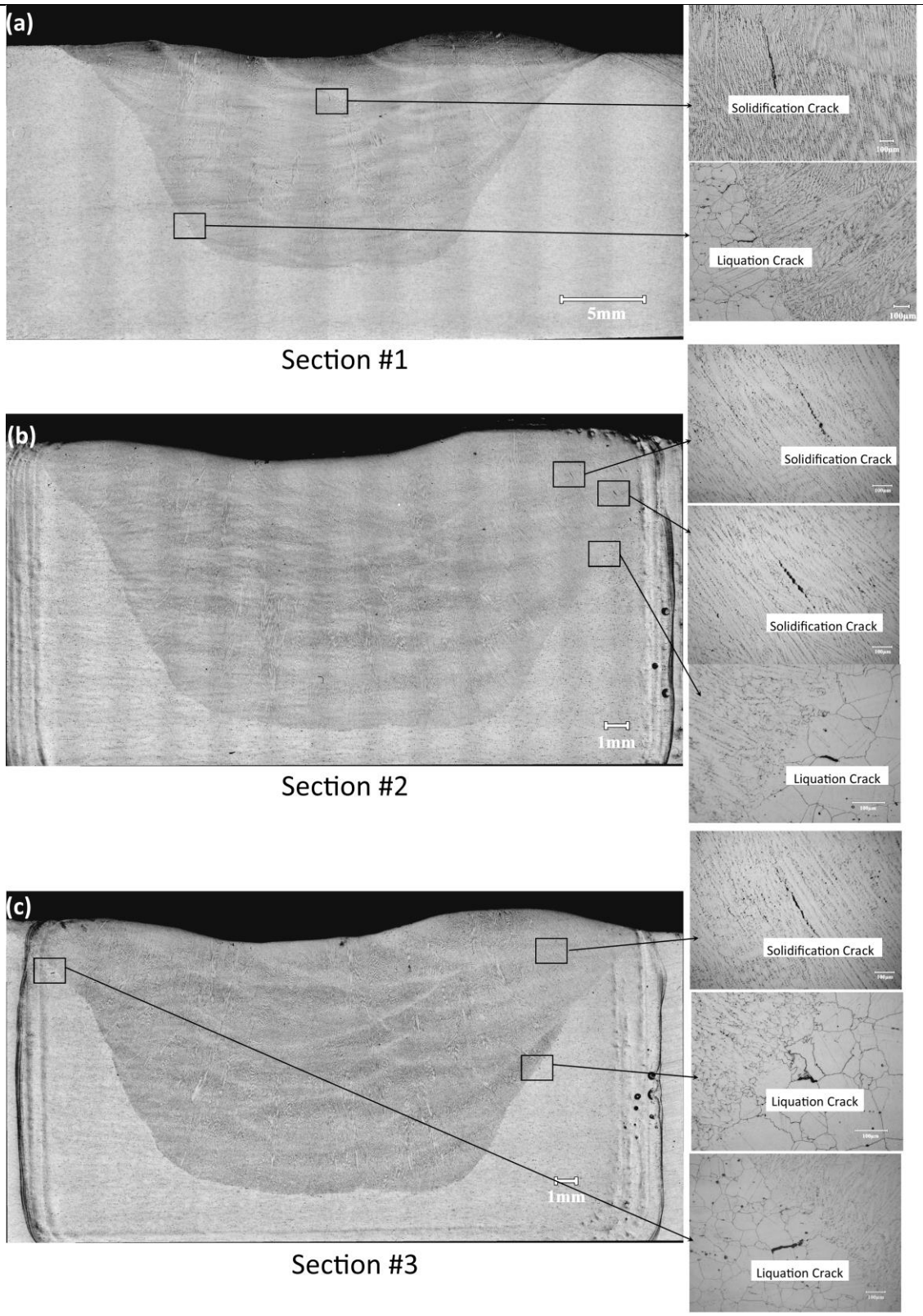

Fig. 8. Additional serial section (about 500 μm were removed between sections) showing weld, Z11116, is not defect-free as would seem to be the case in transverse section of Fig. 7.

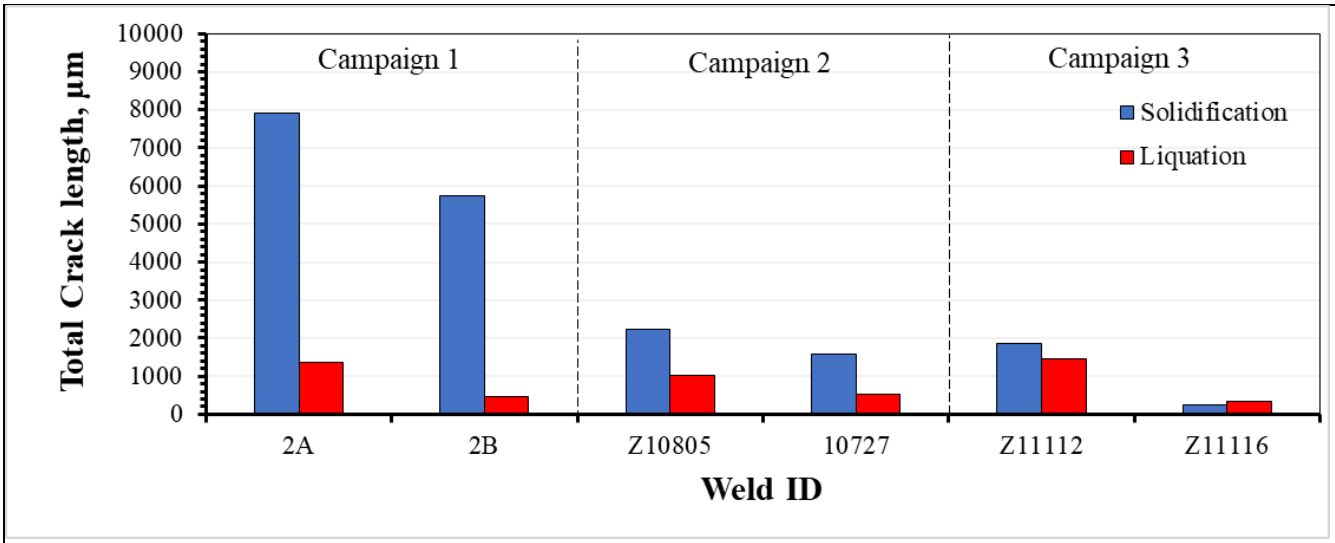

Fig. 9. Plots of the total length of solidification and liquation cracks in transverse sections of the welds as a function of welding campaign. Significant progress has been made on both types of cracks but especially on the solidification cracking issue.

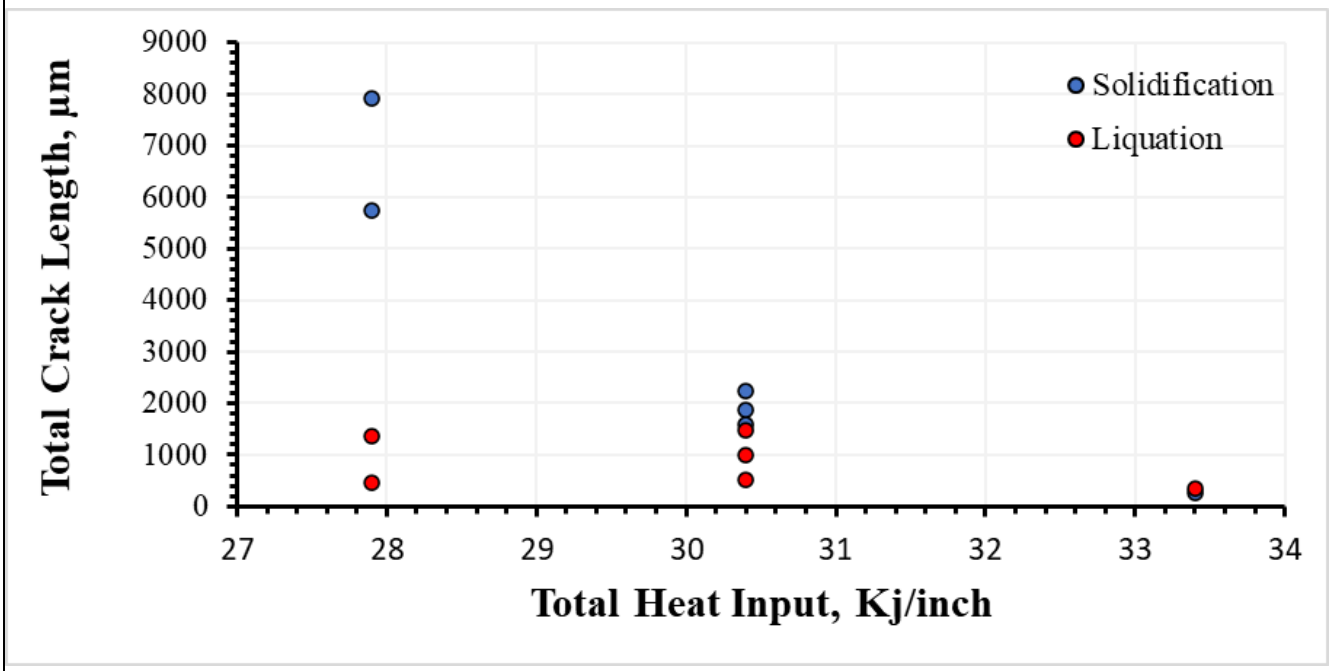

Fig. 10. Total solidification and liquation crack length as a function of heat input from the combined arc and laser energy. Solidification cracking is a strong inverse function of heat input, however, the total liquation crack length does not appear to be a strong function of total heat input.

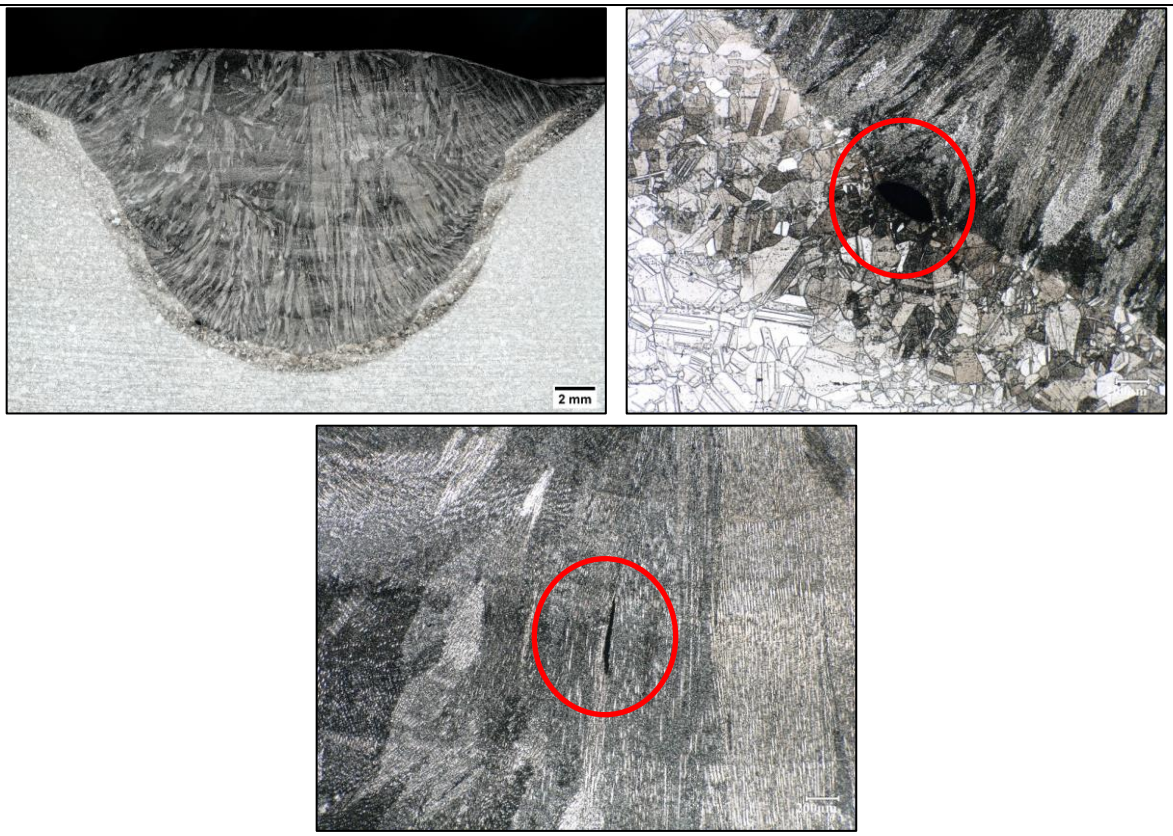

Fig. 11. Multi-pass laser trailing hybrid laser arc weld macrograph using star wobble pattern with 2 kW of laser power (top left). Lack of fusion defect (top right). A single solidification crack, approximately 400 µm in length was also present (bottom). Weld Z20531.

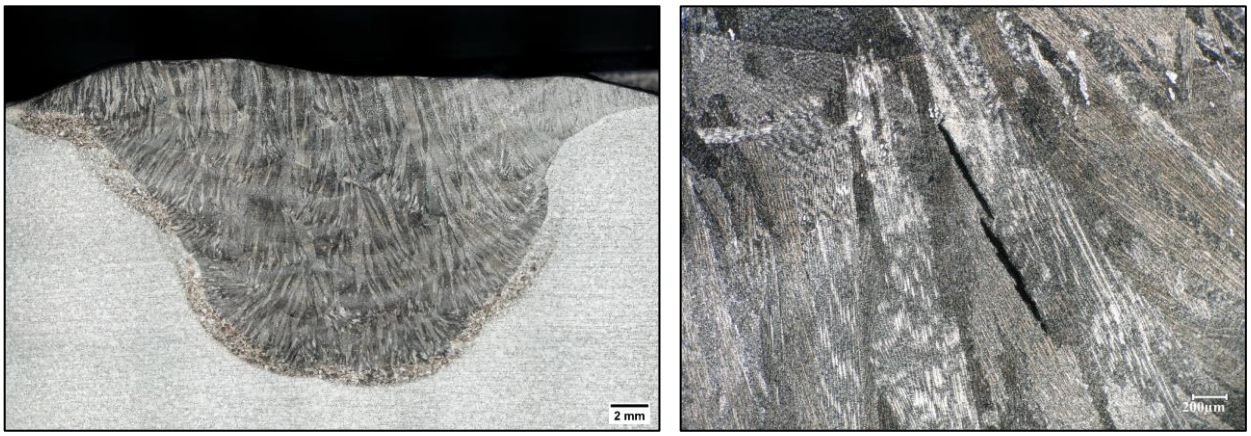

Fig. 12. Multi-pass laser trailing hybrid laser arc weld macrograph using star wobble pattern with 3 kW of laser power (left). A single solidification crack, approximately 800 µm long, was the only defect found in the cross-section (right). Weld Z20606.

Laser decoupling from the arc

In the previous laser trailing study, the laser interacted with the welding arc and was entirely directed into the weld pool. That configuration maintained the hybrid process – where the laser and arc interact for arc stabilization at high travel speeds. This proposed approach further shifts the laser from the arc to the back edge of the weld pool – effectively decoupling the laser from the arc to create a tandem welding process, Fig. 13. It is believed that this method can further alter the fluid flow, change the weld pool shape, and fragment dendrites to promote grain refinement. Therefore, a tandem laser arc approach may eliminate the solidification cracking. Because HAZ liquation cracking was not encountered in the laser trailing HLA welds, it is believed that this will not be an issue with the tandem laser-arc process. If necessary, the travel speed can also be reduced to produce an elliptical shaped weld pool, as compared to a tear-drop shape, which is susceptible to solidification cracking.

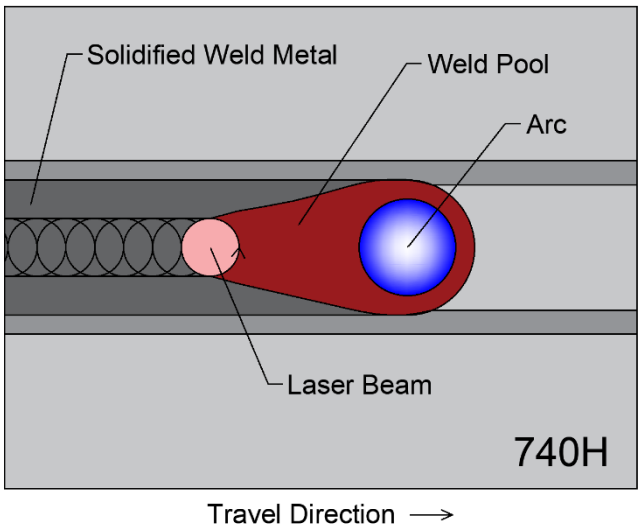

Fig. 13. Schematic showing the tandem laser arc process to stir the trailing edge of the weld pool. Ideally, this will change the fluid flow, modify the weld pool shape, and create grain refinement. All of which can aid in reducing susceptibility to solidification cracking.

Preheating

Preheating base material is a common solution to relieve residual stresses and/or promote desirable microstructures. Preliminary modeling results from PSU show that preheating the base plate will reduce the internal stresses and diminish solidification cracking susceptibility. Benefits were observed at plate temperatures as low as 200°C. The previous HLA welds had interpass temperatures measuring at or below 150°C after the first weld pass. Therefore, this solution proposes evaluating preheat and interpass temperatures near 300°C to alleviate residual stresses. In addition, it may be required to slightly decrease the travel speed to optimize the shape of the weld pool as in the tandem laser-arc process.

Task 5, Complete 3” thick weld (thick land laser weld + HLAW groove filling)

This task has been put on hold until hybrid laser arc welding parameters and/or HLAW configurations can be found that produce welds capable of passing the ASME Boiler and Pressure Vessel Code, Section IX, weld qualification testing.

ISSUES

Lack of a set of HLAW parameters that will produce defect-free welds at this point in the project requires addition (unplanned) HLAW trials which can be costly. It is possible that these trials may use funds originally budgeted for the productivity study as well as the demonstration of this method to join 3” thick plate and Milestones 5 & 6 may not be met within the current budget of the project.

Report Prepared By	Date
Thomas M. Lillo, INL; Tate Patterson, INL; Todd Palmer, PSU	7/28/2022